Tunable critical Casimir forces counteract Casimir–Lifshitz attraction

(article starts on next page)

Tunable critical Casimir forces counteract Casimir–Lifshitz attraction

Falko Schmidt[1,2] ✉, **Agnese Callegari** [1], **Abdallah Daddi-Moussa-Ider** [3,4],
Battulga Munkhbat [5,6], **Ruggero Verre** [5], **Timur Shegai** [5], **Mikael Käll** [5],
Hartmut Löwen[3], **Andrea Gambassi** [7,8] and **Giovanni Volpe** [1] ✉

In developing micro- and nanodevices, stiction between their parts, that is, static friction preventing surfaces in contact from moving, is a well-known problem. It is caused by the finite-temperature analogue of the quantum electrodynamical Casimir–Lifshitz forces, which are normally attractive. Repulsive Casimir–Lifshitz forces have been realized experimentally, but their reliance on specialized materials severely limits their applicability and prevents their dynamic control. Here we demonstrate that repulsive critical Casimir forces, which emerge in a critical binary liquid mixture upon approaching the critical temperature, can be used to counteract stiction due to Casimir–Lifshitz forces and actively control microscopic and nanoscopic objects with nanometre precision. Our experiment is conducted on a microscopic gold flake suspended above a flat gold-coated substrate immersed in a critical binary liquid mixture. This may stimulate the development of micro- and nanodevices by preventing stiction as well as by providing active control and precise tunability of the forces acting between their constituent parts.

Long-range forces emerge between microscopic objects that confine a fluctuating field, irrespective of the field's specific nature. Quantum electrodynamical Casimir forces, for example, act on neighbouring uncharged conducting objects because they effectively confine electromagnetic fluctuations of the quantum vacuum[1]. Their generalization at finite temperature and in material media is known as Casimir–Lifshitz forces[1–3]. Since these forces are almost always attractive[4–6], they can cause the well-known problem of stiction between the various parts of nanodevices, such as those found in microelectromechanical systems (MEMS) and nanoelectromechanical systems (NEMS)[7]. This has motivated several recent studies to search for repulsive Casimir–Lifshitz forces both in vacuum[8–12] and in media[13,14]. Making Casimir–Lifshitz forces repulsive in vacuum requires a careful design of the geometrical shape of the surfaces involved[9,15] and this repulsion is usually possible only along some spatial directions. Experimentally, repulsive forces

have only been obtained for specifically engineered systems, for example, by a careful choice of the materials of the two interacting surfaces and the separating liquid[16–19], by using metamaterials with negative refractive index (which, however, are not readily available[8,20,21]), by coating one of the surfaces with a low-refractive-index material[22] or by adjusting the concentration of ligands in solution[23], while theoretical studies have investigated the possibility of realizing repulsive forces experimentally by employing optically chiral materials in combination with magnetic fields[24]. In any case, these forces do not give rise to stable equilibria[25] and, as a more severe limitation, their magnitude is determined by the properties of the various materials and, in the majority of the cases, cannot be controlled by external parameters. Recently, experimental studies have shown that a combination of attractive and repulsive Casimir–Lifshitz forces can be used to levitate particles away from a surface[22], and that they can trap freely floating particles near

[1]Department of Physics, University of Gothenburg, Gothenburg, Sweden. [2]Institute of Applied Physics, Friedrich-Schiller-University, Jena, Germany. [3]Institut für Theoretische Physik II: Weiche Materie, Heinrich-Heine-Universität Düsseldorf, Düsseldorf, Germany. [4]Abteilung Physik lebender Materie, Max-Planck-Institut für Dynamik und Selbstorganisation, Göttingen, Germany. [5]Department of Physics, Chalmers University of Technology, Gothenburg, Sweden. [6]Department of Photonics Engineering, Technical University of Denmark, Kongens Lyngby, Denmark. [7]SISSA – International School for Advanced Studies, Trieste, Italy. [8]INFN, Sezione di Trieste, Trieste, Italy. ✉e-mail: schmidt.falko@uni-jena.de; giovanni.volpe@physics.gu.se
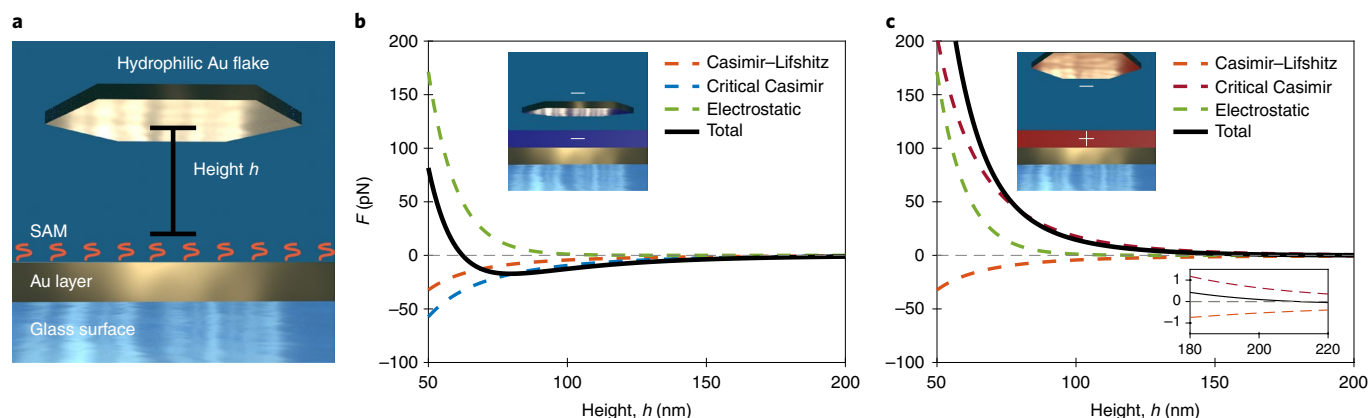
Fig. 1 | Casimir–Lifshitz and critical Casimir forces between parallel plates.
a, Schematic (not to scale) of a hydrophilic (−) gold flake hovering at an equilibrium height h above a glass surface coated with a gold layer and treated with SAMs to control the preferential surface adsorption. **b**, Forces acting on a hydrophilic flake above a hydrophilic (blue layer, inset) surface as a function of its height h. Since the boundary conditions are symmetric (−, −), both the Casimir–Lifshitz forces (dashed orange line, Eq. (5)) and the critical Casimir forces (dashed blue line, Eq. (2) at $\Delta T = T − T_c = −0.1$ K, where T is the solution temperature and T_c is the critical temperature of the critical binary mixture) are attractive. The total force (black line) including also a repulsive electrostatic component (dashed green line) vanishes at $h ≈ 80$ nm. **c**, Forces on a hydrophilic (−) flake above a hydrophobic (+) surface (red layer, top inset) as a function of h. Here, the antisymmetric (−, +) boundary conditions induce a repulsive critical Casimir force (dashed red line, Eq. (2) at $\Delta T = −0.1$ K), while the Casimir–Lifshitz force (dashed orange line, Eq. (5)) remains attractive. Accordingly, the total force vanishes at much larger $h ≈ 210$ nm (bottom inset shows a zoom-in view of this region). The presence of repulsive critical Casimir forces greatly raises the equilibrium height of the flake above the surface. The forces shown in **b** and **c** are calculated for a 34-nm-thick 1,520-nm-wide gold flake suspended in water–2,6-lutidine above a 40-nm-thick gold layer.

surfaces, leading to the formation of Fabry–Pérot cavities when multiple particles assemble on top of each other[23]. Despite these advances in the manipulation of nanoparticles, these systems are inherently static and lack any tunable parameters to allow dynamic control. Although a protocol to dynamically control the Casimir–Lifshitz force was proposed theoretically in ref. [24] by varying the strength and orientation of a magnetic field, its experimental realization is still challenging.

Critical Casimir forces are the thermodynamic analogue of quantum electrodynamical Casimir forces and were first theoretically predicted by Fisher and de Gennes in 1978[26]. They arise, for example, between objects immersed in a binary liquid mixture kept near a second-order phase transition, owing to the confinement of the thermal fluctuations of the local concentration of one of the components of the binary mixture (which is the order parameter of the transition)[27]. In soft matter, thermal fluctuations typically occur on molecular length scales (subnanometre) and, accordingly, the effects they produce are generally negligible at larger separations. However, upon approaching the critical point of a second-order phase transition, the fluctuations become correlated on much longer length scales (up to several microns) and can thus substantially affect the behaviour of microscopic systems[27]. Importantly, critical Casimir forces can be either attractive or repulsive depending on the surface chemistry of the objects involved[28–30]: While the critical Casimir forces between surfaces with similar adsorption preferences (either hydrophilic or hydrophobic) are attractive, they become repulsive when these preferences are opposite.

The first direct experimental measurement of critical Casimir forces was achieved only in 2008[29]: Using total internal reflection microscopy, femtonewton forces were measured on a single spherical microscopic particle suspended above a planar surface in a critical water–lutidine liquid mixture. Since then, these forces have been investigated under various conditions, for example, by varying the properties of the surfaces involved, demonstrating the occurrence of both attractive and repulsive forces[29–31] as well as the existence of many-body effects[32] and the possibility of levitating spherical colloids over patterned substrates solely by critical Casimir forces[33]. The subtle interplay between these forces and the electrostatic interaction in the presence of salt[34–36] or the van der Waals force in nonpolar

fluids[37] have also been investigated. Studies of the phase behaviour of colloidal dispersions in a critical mixture[30,38] have indicated that critical Casimir forces are viable candidates to control the self-assembly of micro- and nanostructures[39–41] and quantum dots[42]. In addition, fluctuation-induced effects similar to critical Casimir forces have been investigated, for example, at the percolation transition of a chemical sol[43], in the presence of temperature gradients[44], in granular fluids[45] and in active matter systems[46,47].

Here we demonstrate experimentally that repulsive critical Casimir forces can be used to compensate for attractive Casimir–Lifshitz forces. In particular, we study a microscopic gold flake diffusing above a gold surface immersed in a critical binary liquid mixture. We control the magnitude of these forces by varying the temperature of the mixture and the attractive/repulsive character of the critical Casimir forces by chemical functionalization of the gold flake and surface, obtaining repulsive forces for opposite surface functionalizations. Far from the critical temperature, we observe stiction between the flake and the surface due to Casimir–Lifshitz forces. However, as we approach the critical temperature, we observe the emergence of repulsive critical Casimir forces that are sufficiently strong to prevent stiction and to release the flake from the surface, above which it then levitates. In addition, we demonstrate that this behaviour is reversible and can be employed to actively control the flake position above a structured surface.

Results
Working principle
We first describe a simple model to clarify how repulsive critical Casimir forces can be employed to counteract attractive Casimir–Lifshitz forces, by estimating theoretically the orders of magnitude of the forces involved. Consider two flat parallel plates (Fig. 1a): One is a thin gold flake (length $a = 1,520$ nm, thickness $b = 34$ nm) suspended in a critical binary liquid mixture above a gold-coated (thickness 40 nm) glass substrate, which is the second plate. The first plate hovers at a height h above the surface because of the interplay of three forces (see details in Methods): the Casimir–Lifshitz force, which, in this case, is attractive; the critical Casimir force, whose character and strength can be varied by modifying the surface functionalization and tuning the solvent

temperature; and the electrostatic force, which provides a short-range repulsion between the flake and the substrate. The gravitational force acting on the flake is negligible compared with the other forces acting on the flake in close proximity to the substrate.

The attractive Casimir–Lifshitz force between two plates depends on h as

$$F_{CL}(h) = -\frac{dG_{CL}}{dh} S, \qquad (1)$$

where G_{CL} is the Casimir–Lifshitz free energy per unit area of the system and S is the area of the flake (ref. [48] and Methods). In this case, the force depends on the thicknesses of the flake and of the gold layer deposited on the glass surface, as well as on the dielectric properties of the glass and of the solvent (Methods and Extended Data Fig. 1). The resulting Casimir–Lifshitz forces are plotted as dashed orange lines in Fig. 1b,c for two opposite surface treatments of the gold layer.

The critical Casimir forces are induced by the confinement of the critical mixture between the flake and the substrate. Their strength F_{crit} depends on the adsorption preference of the surfaces involved and on the difference $\Delta T = T - T_c$ between the actual temperature T of the binary liquid mixture and its critical temperature T_c. In particular,

$$F_{crit}(h, \Delta T) = -\frac{k_B T_c}{h^3} \, \theta\left(h/\xi(\Delta T)\right) S, \qquad (2)$$

where $\xi(\Delta T)$ is the correlation length of the fluctuations of the order parameter of the mixture depending on ΔT and $\theta\left(h/\xi(\Delta T)\right)$ is a universal scaling function[27]. For the sake of simplicity, in the following we omit the explicit dependence on ΔT of ξ. Whether the critical Casimir forces are repulsive or attractive depends on the boundary conditions given by the surface preferential adsorption of one of the two components of the mixture (indicated by "−" or "+"). We can control these boundary conditions by chemically functionalizing the surfaces with appropriate self-assembled monolayers (SAMs) (Methods). In the case of symmetric boundary conditions (−, −) or (+, +) (that is, the flake and surface prefer the same component of the mixture), the critical Casimir forces are attractive (Fig. 1b, dashed blue line). For antisymmetric boundary conditions (−, +) (that is, preference for different components), the critical Casimir forces are repulsive (Fig. 1c, dashed red line).

The electrostatic repulsive force F_{ES} is due to the double layer of counterions in close proximity to the surface of the flake and the substrate[49]. According to the Derjaguin–Landau–Verwey–Overbeek (DLVO) theory (neglecting boundary effects), we have

$$F_{ES}(h) = P_0 \, e^{-h/\lambda_D} S, \qquad (3)$$

where λ_D is the Debye screening length of the critical mixture and P_0 is a parameter with the dimensions of pressure.

The theoretical predictions presented in Fig. 1b,c show that, in the configuration we consider at $\Delta T = -0.1$ K, the magnitude of the critical Casimir forces is expected to be larger than that of the Casimir–Lifshitz forces, so we can use the critical Casimir forces to tune the equilibrium position of the flake above the surface. In the case of asymmetric boundary conditions (−, +) (Fig. 1c), this provides an additional repulsion between the flake and surface, which can be used to prevent stiction.

Experimental setup and analysis

In the experiment, we consider a gold flake suspended in a near-critical water–2,6-lutidine mixture (lutidine critical concentration $c_L^c = 0.286$ mass fraction, lower critical temperature $T_c \approx 310$ K, that is, 34 °C) above a gold-coated surface (Fig. 1a). The gold flakes are fabricated using a wet chemical synthesis method[50] that produces single-crystalline gold flakes (diameter $d = 3 \pm 2$ μm), stabilized by cetrimonium bromide

(CTAB) ligand molecules, with average thickness of $b = 34 \pm 10$ nm in aqueous solution[23] and of various geometrical shapes (scanning electron microscopy image in Fig. 2a and details in Methods). These flakes are hydrophilic due to the formation of a CTAB bilayer on their surface[51]. For this study, we select flakes with the shape of equilateral hexagons (Fig. 2b, inset) owing to their larger degree of symmetry.

The substrate is constituted by a glass slide on which a 35-nm-thick gold coating is deposited by sputtering. To control the surface preferential adsorption, the gold coating is chemically functionalized by a SAM of either hydrophilic or hydrophobic thiols by immersing the surface in a 1 mM thiol solution with different end groups (Methods)[52]. We tune the temperature of the sample via a two-stage feedback temperature controller with ±20 mK stability[32,53] and thus control the strength of the critical Casimir forces.

As anticipated by our theoretical predictions (Fig. 1 and discussion above), a change in the magnitude or sign of the critical Casimir force acting on the flake alters its equilibrium height h above the surface. However, these changes are on the order of a few tens of nanometres and, thus, difficult to measure directly. A more convenient approach consists in measuring the lateral diffusion of the flakes along the substrate, which depends sensitively on their height[54–56]: the higher (lower) the flake is above the surface, the larger (smaller) its diffusion is. Accordingly, we record a video of the flake's motion for a long period of time (~100 s, with a sample rate of 100 Hz) using a bright-field microscope (Extended Data Fig. 2). Using digital video microscopy, we reconstruct the projection of the flake's position on the x–y plane, where x and y are the Cartesian coordinates along the surface of the substrate (Fig. 2b, solid line and Supplementary Video 1). The flake diffuses freely along the x–y plane, while its motion along the z-direction (perpendicular to the substrate) is negligible. From the x–y trajectory, we calculate the mean square displacement (MSD(t) at time t in Fig. 2c), which, for a freely diffusing flake, grows as MSD(t) = $4Dt$, where D is the diffusion constant. D can be obtained by fitting the measured MSD (Methods). Since D depends sensitively on h, its value can be used to infer the equilibrium position h of the flake above the surface. We have calibrated the theoretical reference $D(h)$ (Fig. 2d, blue line) using hydrodynamic simulations of the flake (Methods), which permit a determination of the equilibrium height of the flake with nanometre (±1.3 nm) precision (Fig. 2d, black dashed lines). In addition, we validated the indirect measurement of h obtained as described above by alternatively measuring the Fabry–Pérot cavity modes (Supplementary Information Section II). In fact, a microcavity is formed between the flake and the gold substrate. We measure its reflectivity spectrum to determine the spatial variation of the cavity thickness using a spectrometer (Methods and Extended Data Fig. 3)[23]. The measured cavity modes in the reflection spectrum at different positions were analysed by the standard transfer matrix method[23]. We find that the flake is about 90 ± 10 nm away from the surface inside a critical water–2,6-lutidine mixture at $\Delta T = -0.5$ K, independently of the actual surface functionalization, and this value is in good agreement with our measurements of $h = 100$ nm using hydrodynamic simulations.

Measurement of the Casimir–Lifshitz force

Using the method described in the previous section, we can investigate the separate effects of the various forces on the flake. We start by determining the (attractive) Casimir–Lifshitz force at low temperature $\Delta T \approx -1$ K, at which the critical Casimir force is negligible (importantly, the Casimir–Lifshitz force and the electrostatic force are not substantially affected by a temperature change up to several kelvin, because they are expected to be smooth functions of the absolute temperature T, whose value changes by less than 1% in our experiment). The Casimir–Lifshitz force can then be determined by comparing the total force (which includes electrostatics) acting on the gold flake above the uncoated glass surface (where the Casimir–Lifshitz force is weak) and the force acting when the flake is above a gold-coated surface. In fact, we observe that the
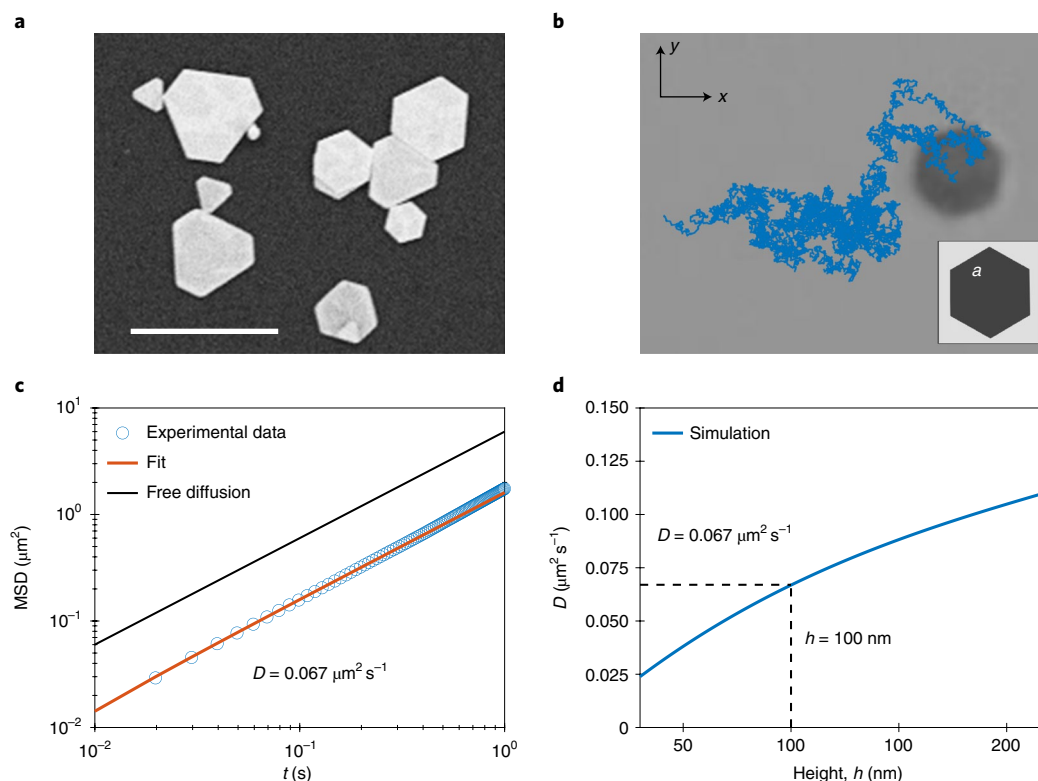
a, **b**

c, **d**

Fig. 2 | Hydrodynamic measurement of flake height above the substrate.
a, Scanning electron microscopy image of gold flakes with various sizes and
shapes. The scale bar corresponds to 5 μm. **b**, Microscope image and trajectory
(blue) recorded for 100 s of a diffusing flake shaped as an equilateral hexagon
with side $a = 840$ nm (inset) in a critical water–2,6-lutidine mixture at $\Delta T = -0.5$ K
(Supplementary Video 1). **c**, Experimental data (blue circles) and theoretical fit
(orange line) of the mean square displacement (MSD) of the flake's trajectory

in **b**, which provides an estimate of the diffusion constant $D = 0.067$ μm^2 s^{-1},
compared with $D \approx 5.98$ μm^2 s^{-1} for free diffusion (black line). The s.d. of the
experimental points is much smaller than the symbols. **d**, Theoretical diffusion
D of a hexagonal flake with side $a = 840$ nm as a function of its height h above
the surface (Fig. 1a) obtained from hydrodynamic simulations (see Methods
and Supplementary Information Section IV). The experimentally measured
$D = 0.067$ μm^2 s^{-1} corresponds to height $h = 100$ nm.

flake suspended above an uncoated glass surface hovers at $h \approx 300$ nm
(Extended Data Fig. 4), while its equilibrium height reduces to $h \approx 100$ nm,
when the flake is floating above the gold-coated surface. This fact is
largely independent of the gold functionalization and, therefore, of
the adsorption properties of the surface (as seen from the values of h
at low temperature, $\Delta T = -1$ K, in Fig. 3b,e). This reduction of the value
of h is the result of the presence of attractive Casimir–Lifshitz forces
between the gold flake and the gold surface[57]. Further evidence of the
nature of this force is provided by the quality of the fit of the experimental
data with the theoretical model (Extended Data Fig. 5). In particular, we
compare the inferred heights with the theoretical average height of the
flake floating above the gold-coated and uncoated silica surface. This fit
allows us to infer the parameters of the electrostatic interaction in the
two cases, which are important for the theoretical interpretation of the
experimental results provided in the following two subsections. The
details of the fitting procedure are given in Methods.

Interplay between critical Casimir and Casimir–Lifshitz forces
As seen in Fig. 1c, repulsive critical Casimir forces are theoretically
expected to be able to overcome Casimir–Lifshitz forces in magnitude
as the solvent's temperature approaches T_c. In this section, we provide
experimental evidence for this fact.

In Fig. 3a–c, we consider a hexagonal hydrophilic flake with
$a = 700$ nm (Fig. 2b) above a hydrophilic surface, realizing symmet-
ric (−, −) boundary conditions. As the temperature of the solution is
increased towards T_c, the flake's diffusion constant D decreases from
~0.09 μm^2 s^{-1} to 0.07 μm^2 s^{-1} (blue squares in Fig. 3a), indicating that
the flake's distance from the substrate decreases from 108 ± 7 nm to

68 ± 5 nm (Fig. 3b, blue squares). This decrease is primarily due to an
increasingly stronger critical Casimir force (Fig. 3c, blue symbols), but
also to an increase of the Casimir–Lifshitz force (Fig. 3c, orange crosses)
as the equilibrium distance h_{eq} of the flake decreases. The experimental
results agree well with theoretical predictions for the Casimir–Lifshitz
forces (Fig. 3c, solid orange line), the critical Casimir forces (Fig. 3c,
solid blue line), the electrostatic force (Fig. 3c, solid green line) and
the resulting height of the flake (Fig. 3b, solid blue line) (Methods). We
emphasize that the magnitude of the critical Casimir forces acting on
the flake becomes larger than that of the Casimir–Lifshitz forces when
the temperature is sufficiently close to T_c (that is, $\Delta T > -0.3$ K) (Fig. 3c).

In Fig. 3d–f, we consider the case of a hexagonal hydrophilic flake
with $a = 840$ nm above a hydrophobic surface realizing antisymmetric
(−, +) boundary conditions. Interestingly, while the sizes of the two
flakes are different, their equilibrium heights $h_{eq} \approx 100$ nm far from T_c
are similar, confirming that the forces acting per unit area are similar
and not affected by the critical Casimir contribution, which would
have opposite signs for the two flakes. In this case, however, as the
temperature approaches T_c, the flake's diffusion constant D increases
(Fig. 3d, red circles) from ~0.067 μm^2 s^{-1} to ~0.15 μm^2 s^{-1}, indicating
that its equilibrium height h_{eq} above the surface increases (Fig. 3e, red
circles). In particular, h_{eq} changes from 96 ± 10 nm at $\Delta T = -0.9$ K to
196 ± 47 nm at $\Delta T = -0.1$ K. This increase is primarily due to the emer-
gence of repulsive critical Casimir forces (Fig. 3f, red circles), combined
with the decrease of the magnitude of the Casimir–Lifshitz forces
(Fig. 3f, orange circles) as a consequence of the larger distance between
the flake and the substrate. These experimental results fit well with the
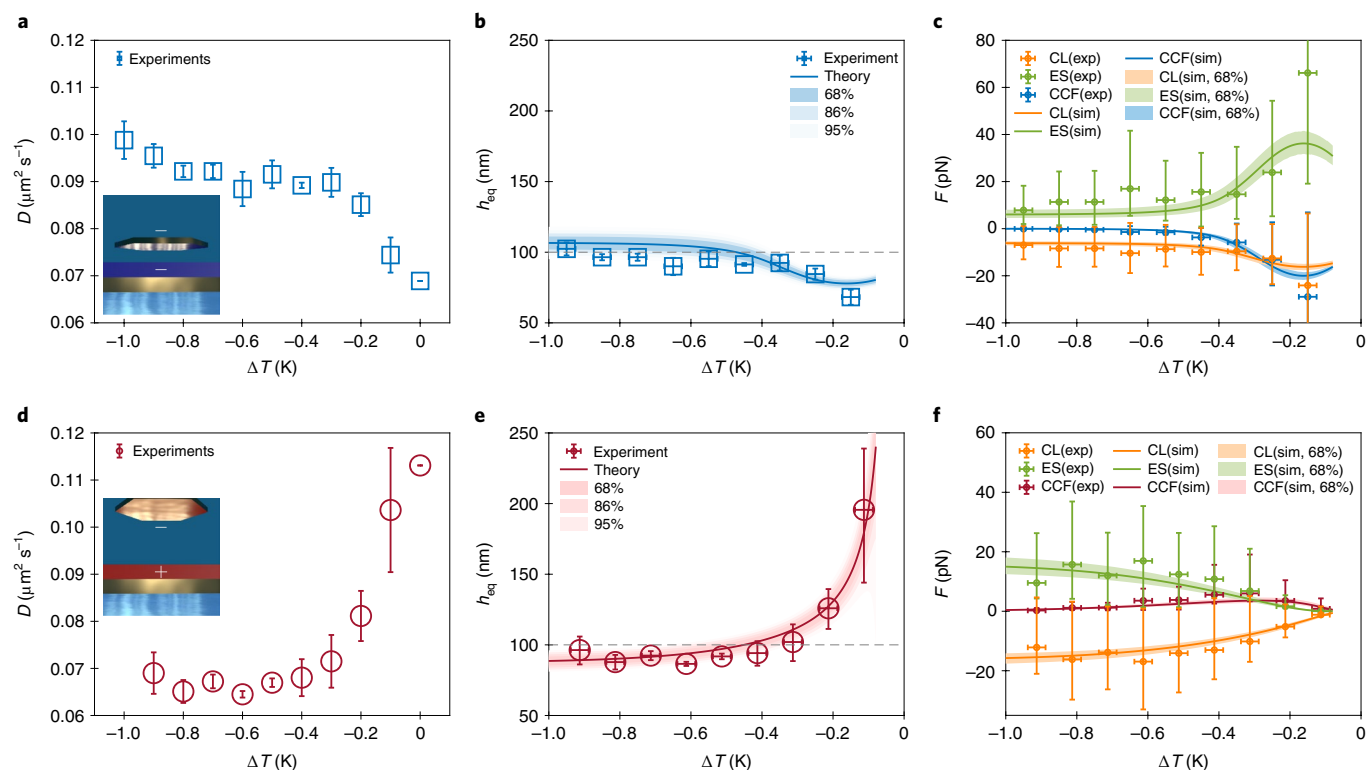theoretical predictions (Fig. 3e,f, solid lines) (Methods). Also for this

Fig. 3 | Critical Casimir forces overcome Casimir–Lifshitz forces. a,b, The diffusion constant D of a hydrophilic hexagonal flake with $a = 700$ nm above a hydrophilic surface (symmetric (−, −) boundary conditions) decreases as the temperature T approaches the critical temperature T_c (**a**, blue squares) while its height h decreases (**b**, blue squares). The solid blue line is the best fit of the theoretical model (Eq. (8)), from which we extracted h_{eq} in Eq. (9). **c,** The flake is under the action of the Casimir–Lifshitz (CL) force (orange dots) and the critical Casimir force (CCF, blue dots), both of which are attractive and whose strengths increase as the flake approaches the surface, while electrostatic forces (ES, green dots) are repulsive. The orange and blue solid lines are the theoretical (sim) fits of the critical Casimir (Eq. (2)) and Casimir–Lifshitz (Eq. (1)) forces, respectively. exp, experiment; sim, simulation. Note how the critical Casimir force becomes stronger than the Casimir–Lifshitz force at $\Delta T \approx -0.3$ K. **d,e,** The diffusion constant D (red circles) for a hydrophilic hexagonal flake with $a = 840$ nm above

a hydrophobic surface (antisymmetric (−, +) boundary conditions) increases upon approaching T_c (**d**) as its height h (red circles) increases (**e**). **f,** The solid red line is the best fit of the theoretical model (Eq. (8)) of the average height $h_{eq} \approx \langle h \rangle$ (Eq. (9)) under the action of the Casimir–Lifshitz force (orange dots, attractive), the critical Casimir force (red dots, repulsive) and the electrostatic force (green dots, repulsive). The red, orange and green solid lines are the theoretical values from the fit of the critical Casimir, Casimir–Lifshitz and electrostatic forces, respectively. Data presented as mean values. The error bars on the experimental points in **b** and **e** are the s.d. from three measurements. The error range for the theoretical lines in **b** and **e** is indicated as shaded areas for the confidence levels of 68%, 86% and 95%. In **c** and **f**, only the 68% confidence level error range is shown. The dashed lines in **b** and **e** refer to the equilibrium height of particle far away from criticality.

case of antisymmetric boundary conditions, the magnitude of the critical Casimir forces eventually exceeds that of the Casimir–Lifshitz force. Interestingly, at $\Delta T \approx -0.1$ K, the equilibrium height h_{eq} is increased to a value at which the electrostatic repulsion becomes negligible, the weight of the flake is still much smaller than the Casimir–Lifshitz attraction at that distance and thus the attraction of the Casimir–Lifshitz force is essentially balanced by the repulsive critical Casimir force. The electrostatic repulsion in the two cases with different boundary conditions is found to be essentially the same by the fitting procedure (Methods). Thus, this experiment demonstrates that the repulsive critical Casimir forces, as the only tunable repulsive force in the system, can effectively overcome the Casimir–Lifshitz attraction upon approaching the critical temperature T_c. Note that, in this case, the presence of the electrostatic force is not necessary to prevent stiction, at least close to the critical point. On the other hand, the electrostatic repulsion may be fundamental to avoid stiction when far from criticality or in the presence of attractive critical Casimir forces.

Spatio-temporal control

In the following, we show experimentally how a particle confined to a metallic surface by Casimir–Lifshitz attraction can be lifted away from

the substrate by the repulsive critical Casimir force and, therefore, start diffusing freely. For this simple, proof-of-principle experiment we fabricated gold stripes (width 3 μm) separated by gaps of glass of the same width (Fig. 4a). We treated the glass stripes and the gold stripes with SAMs having opposite wetting properties to make them hydrophilic and hydrophobic, respectively. A hydrophilic gold flake ($a = 1450$ nm) is floating above this configuration. The size of the flake is indicated in Fig. 4a and is comparable to the stripe width. Accordingly, symmetric boundary conditions (−, −) are realized when the flake is entirely above the glass stripes, while the boundary conditions are antisymmetric (+, −) when it is entirely above the gold stripes. To study the interplay between the Casimir–Lifshitz forces and the critical Casimir forces, the temperature of the mixture is modulated periodically in time (Fig. 4a, inset). At temperatures far below T_c, that is, with $\Delta T \approx -1.5$ K, the flake is essentially confined on the gold stripes by the Casimir–Lifshitz forces, as shown by its trajectory (Fig. 4b, white line). In fact, one observes experimentally that the flake cannot escape from the gold stripe even at long times, up to tens of minutes. This behaviour reveals the presence of an energy barrier that prevents the flake from moving to the neighbouring glass stripes. In agreement with the results shown in Section 2.4, we know that the flake hovers at an equilibrium height
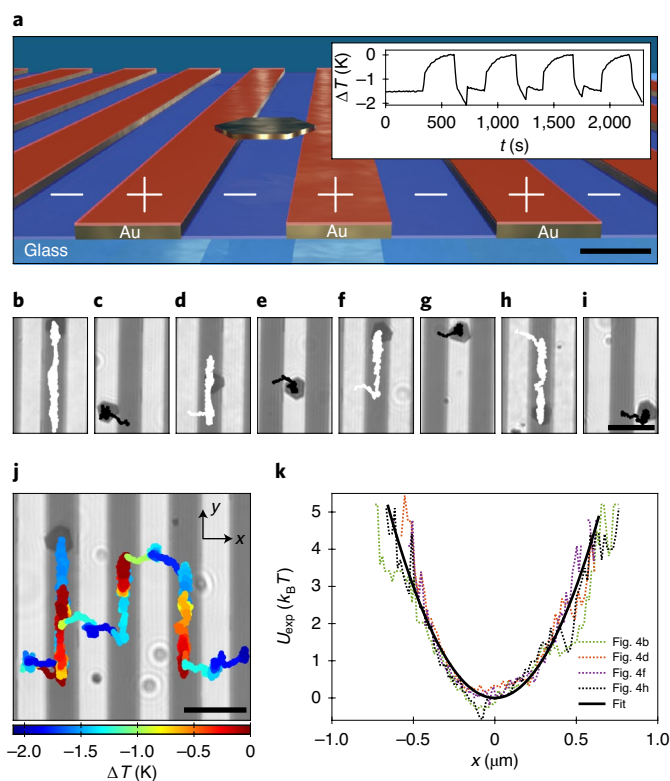
Fig. 4 | Trapping and release of a flake. a, Hydrophobic gold stripes (thickness 30 nm, width 3 μm, separation 3 μm) nanofabricated on a hydrophilic glass substrate with a hydrophilic gold flake (a = 1,450 nm) floating above. Inset: periodic raising and lowering of the temperature T to and away from the critical temperature T_c. The black scale bar corresponds to 2 μm. **b–i**, Trajectories of a hydrophilic gold flake when T is appreciably below T_c (white trajectories) so that the Casimir–Lifshitz force dominates and confines the flake over the gold stripes (dark stripes in background images) (**b,d,f,h**) and when $T \approx T_c$ (black trajectories) so that the critical Casimir force emerges, repelling the flake from the gold stripes to the glass regions (light stripes in background images) (**c,e,g,i**). **j**, Full trajectory of the flake under periodic heating and cooling of the sample, showing that transitions occur shortly after reaching $T \approx T_c$ (Supplementary Video S2). Its starting point is marked by the particle image. Scale bars 6 μm. **k**, Casimir–Lifshitz potential U_{exp} along the x-direction (see axes in **j**) in case of a trapped flake above gold stripes. The dotted lines represent the experimentally measured potentials for the trajectories in **b**, **d**, **f** and **h**, while the solid line represents the fitting to a harmonic potential with trap stiffness $k_x \approx 0.1$ pN μm^{-1}.

$h_{eq} \approx 100$ nm over the gold substrate for $\Delta T \lesssim -0.5$ K. Instead, when T is increased towards T_c, repulsive critical Casimir forces emerge and lift the flake away from the gold stripe, similar to what we observed experimentally in Fig. 3e. Thus, the flake diffuses freely away from the gold stripe and, eventually, reaches the glass stripe. Here, owing to the symmetric boundary conditions, it is attracted towards the glass by the presence of the attractive critical Casimir forces (Fig. 4c). Only after decreasing T far below T_c, does the critical Casimir force diminish sufficiently for the flake to get attracted and trapped onto a gold stripe again.

This cycle can be repeated by adjusting the temperature of the system, resulting in continuous transitions between gold and glass stripes (Fig. 4b–i and Supplementary Video S2). The complete trajectory is shown in Fig. 4j, which is colour coded based on the measured temperature. It can be seen that the transitions between adjacent stripes occur only after T_c (dark red) has been reached.

This experimental behaviour can be explained by a theoretical model discussed in detail in Supplementary Information Section III.

In the theoretical model describing a flake suspended on a substrate coated with gold stripes, the flake is subject to a potential $U_{tot}(\Delta T; x, h)$ (Extended Data Fig. 6a–h), which is a periodic function of the coordinate x of the centre of the flake along the direction perpendicular to the stripes. As discussed in detail in Supplementary Information Section III, the dynamics of the suspended flake along the x direction for a fixed ΔT is ruled by an effective potential $U_{eff}(\Delta T; x)$ (Extended Data Fig. 6i–p). For $\Delta T \lesssim -1$ K, the minimum of U_{eff} is located in the middle of the gold stripe (Extended Data Fig. 6i), where the probability density distribution $P_{eff}(\Delta T; x)$ (Eq. (S9)) has a sharp peak (Extended Data Fig. 6q). Upon decreasing ΔT, the peak of P_{eff} becomes less pronounced, though remaining localized at the centre of the gold stripe. Eventually, for $\Delta T \approx -0.1$ K, the probability distribution develops two comparable peaks (Extended Data Fig. 6v), the second being localized at the centre of the silica stripe. For $\Delta T \gtrsim -0.08$ K, this second peak becomes predominant (Extended Data Fig. 6x), in agreement with previous results in literature[33,58,59].

The stiffness of the lateral Casimir–Lifshitz force trapping the flake on the gold stripe when $T \ll T_c$ can be quantified by measuring the effective attractive potential to which the flake is subject. This is done by calculating the probability distribution $P_{exp}(x)$ of the x-component of the trajectories shown in Fig. 4b,d,f,h, from which the effective potential $U_{exp}(x)$ is determined by inverting the Boltzmann factor, that is, $U_{exp}(x) = -k_B T \ln(P_{exp}(x))$. The resulting experimental potentials (Fig. 4k, dashed lines) are then fitted to a harmonic potential $U(x) = kx^2/2$ (Fig. 4k, solid black line) with stiffness $k \approx 0.1$ pN μm^{-1}. Comparing with the theoretical model (Extended Data Fig. 7), we see that we can obtain a value of the stiffness on the same order of magnitude for an appropriate range of the flake's size.

Conclusions and outlook

Our method provides a novel way of controlling the distances of micro- and nanostructures using tunable critical Casimir forces to counteract forces such as the Casimir–Lifshitz force, thereby preventing stiction and device failure. Due to the simplicity of our design—which does not require additional external actions such as that of magnetic fields—the concept can be easily adapted to already existing MEMS and NEMS. Moreover, this path opens up new possibilities for the dynamic control of MEMS and NEMS where the temperature of the system could be controlled via light illumination, enabling faster transitions and higher selectivity for a new generation of the micromembranes that are found ubiquitously in MEMS and NEMS devices.

Online content

Any methods, additional references, Nature Research reporting summaries, source data, extended data, supplementary information, acknowledgements, peer review information; details of author contributions and competing interests; and statements of data and code availability are available at https://doi.org/10.1038/s41567-022-01795-6.

References

1. Casimir, H. B. G. & Polder, D. The influence of retardation on the London–van der Waals forces. *Phys. Rev.* **73**, 360–372 (1948).
2. London, F. The general theory of molecular forces. *Trans. Faraday Soc.* **33**, 8b–26 (1937).
3. Lifshitz, E. M. The theory of molecular attractive forces between solids. *Sov. Phys. JETP* **2**, 73–83 (1956).
4. Kenneth, O. & Klich, I. Opposites attract: a theorem about the Casimir force. *Phys. Rev. Lett.* **97**, 160401 (2006).
5. Bachas, C. P. Comment on the sign of the Casimir force. *J. Phys. A* **40**, 9089–9096 (2007).
6. Dzyaloshinskii, I. E., Lifshitz, E. M. & Pitaevskii, L. P. The general theory of van der Waals forces. *Adv. Phys.* **10**, 165–209 (1961).
7. Maluf, N. & Williams, K. *Introduction to Microelectromechanical Systems Engineering* (Artech House, 2004).

8. Leonhardt, U. & Philbin, T. G. Quantum levitation by left-handed metamaterials. *New J. Phys.* **9**, 254 (2007).

9. Levin, M., McCauley, A. P., Rodriguez, A. W., Reid, M. T. H. & Johnson, S. G. Casimir repulsion between metallic objects in vacuum. *Phys. Rev. Lett.* **105**, 090403 (2010).

10. Milton, K. A. et al. Repulsive Casimir and Casimir–Polder forces. *J. Phys. A* **45**, 374006 (2012).

11. Inui, N. Quantum levitation of a thin magnetodielectric plate on a metallic plate using the repulsive Casimir force. *J. Appl. Phys.* **111**, 074304 (2012).

12. Camacho, M. et al. Engineering Casimir interactions with epsilon-near-zero materials. *Phys. Rev. A* **105**, L061501 (2022).

13. Inui, N. Diamagnetic effect on the Casimir force. *Phys. Rev. A* **83**, 032513 (2011).

14. Pappakrishnan, V. K., Mundru, P. C. & Genov, D. A. Repulsive Casimir force in magnetodielectric plate configurations. *Phys. Rev. B* **89**, 045430 (2014).

15. Abrantes, P. P., França, Y., da Rosa, F. S. S., Farina, C. & de Melo e Souza, R. Repulsive van der Waals interaction between a quantum particle and a conducting toroid. *Phys. Rev. A* **98**, 012511 (2018).

16. Hutter, J. L. & Bechhoefer, J. Manipulation of van der Waals forces to improve image resolution in atomic-force microscopy. *J. Appl. Phys.* **73**, 4123–4129 (1993).

17. Munday, J. N., Capasso, F. & Parsegian, V. A. Measured long-range repulsive Casimir–Lifshitz forces. *Nature* **457**, 170–173 (2009).

18. Van Zwol, P. & Palasantzas, G. Repulsive Casimir forces between solid materials with high-refractive-index intervening liquids. *Phys. Rev. A* **81**, 062502 (2010).

19. Esteso, V., Carretero-Palacios, S. & Míguez, H. Nanolevitation phenomena in real plane-parallel systems due to the balance between Casimir and gravity forces. *J. Phys. Chem. C* **119**, 5663–5670 (2015).

20. Zhao, R., Zhou, J., Koschny, T., Economou, E. & Soukoulis, C. Repulsive Casimir force in chiral metamaterials. *Phys. Rev. Lett.* **103**, 103602 (2009).

21. Dou, M., Lou, F., Boström, M., Brevik, I. & Persson, C. Casimir quantum levitation tuned by means of material properties and geometries. *Phys. Rev. B* **89**, 201407 (2014).

22. Zhao, R. et al. Stable Casimir equilibria and quantum trapping. *Science* **364**, 984–987 (2019).

23. Munkhbat, B., Canales, A., Küçüköz, B., Baranov, D. G. & Shegai, T. O. Tunable self-assembled Casimir microcavities and polaritons. *Nature* **597**, 214–219 (2021).

24. Jiang, Q.-D. & Wilczek, F. Chiral Casimir forces: repulsive, enhanced, tunable. *Phys. Rev. B* **99**, 125403 (2019).

25. Rahi, S. J., Kardar, M. & Emig, T. Constraints on stable equilibria with fluctuation-induced (Casimir) forces. *Phys. Rev. Lett.* **105**, 070404 (2010).

26. Fisher, M. E. & de Gennes, P. G. Wall phenomena in a critical binary mixture. *C. R. Séances Acad. Sci. Ser. B* **287**, 207–209 (1978).

27. Gambassi, A. The Casimir effect: from quantum to critical fluctuations. *J. Phys. Conf. Ser.* **161**, 012037 (2009).

28. Fukuto, M., Yano, Y. F. & Pershan, P. S. Critical Casimir effect in three-dimensional Ising systems: measurements on binary wetting films. *Phys. Rev. Lett.* **94**, 135702 (2005).

29. Hertlein, C., Helden, L., Gambassi, A., Dietrich, S. & Bechinger, C. Direct measurement of critical Casimir forces. *Nature* **451**, 172–175 (2008).

30. Gambassi, A. et al. Critical Casimir effect in classical binary liquid mixtures. *Phys. Rev. E* **80**, 061143 (2009).

31. Gambassi, A. & Dietrich, S. Critical Casimir forces steered by patterned substrates. *Soft Matter* **7**, 1247–1253 (2011).

32. Paladugu, S. et al. Nonadditivity of critical Casimir forces. *Nat. Commun.* **7**, 11403 (2016).

33. Tröndle, M., Kondrat, S., Gambassi, A., Harnau, L. & Dietrich, S. Critical Casimir effect for colloids close to chemically patterned substrates. *J. Chem. Phys.* **133**, 074702 (2010).

34. Nellen, U. et al. Salt-induced changes of colloidal interactions in critical mixtures. *Soft Matter* **7**, 5360–5364 (2011).

35. Bier, M., Gambassi, A., Oettel, M. & Dietrich, S. Electrostatic interactions in critical solvents. *Europhys. Lett.* **95**, 60001 (2011).

36. Pousaneh, F., Ciach, A. & Maciołek, A. How ions in solution can change the sign of the critical Casimir potential. *Soft Matter* **10**, 470–483 (2014).

37. Valchev, G. & Dantchev, D. Critical and near-critical phase behavior and interplay between the thermodynamic Casimir and van der Waals forces in a confined nonpolar fluid medium with competing surface and substrate potentials. *Phys. Rev. E* **92**, 012119 (2015).

38. Maciołek, A. & Dietrich, S. Collective behavior of colloids due to critical Casimir interactions. *Rev. Mod. Phys.* **90**, 045001 (2018).

39. Nguyen, T. A., Faber, S., Hu, Z., Wegdam, G. & Schall, P. Controlling colloidal phase transitions with critical Casimir forces. *Nat. Commun.* **4**, 1584 (2013).

40. Nguyen, D. V., Dang, M. T., Nguyen, T. A. & Schall, P. Critical Casimir forces for colloidal assembly. *J. Condens. Matter Phys.* **28**, 043001 (2016).

41. Nguyen, T. A. et al. Switching colloidal superstructures by critical Casimir forces. *Adv. Mater.* **29**, 1700819 (2017).

42. Marino, E., Kodger, T. E., ten Hove, J. B., Velders, A. H. & Schall, P. Assembling quantum dots via critical Casimir forces. *Sol. Energy Mater. Sol. Cells* **158**, 154–159 (2016).

43. Gnan, N., Zaccarelli, E. & Sciortino, F. Casimir-like forces at the percolation transition. *Nat. Commun.* **5**, 3267 (2014).

44. Najafi, A. & Golestanian, R. Forces induced by nonequilibrium fluctuations: the Soret–Casimir effect. *Europhys. Lett.* **68**, 776–782 (2004).

45. Cattuto, C., Brito, R., Marconi, U. M. B., Nori, F. & Soto, R. Fluctuation-induced Casimir forces in granular fluids. *Phys. Rev. Lett.* **96**, 178001 (2006).

46. Ray, D., Reichhardt, C. & Reichhardt, C. J. O. Casimir effect in active matter systems. *Phys. Rev. E* **90**, 013019 (2014).

47. Lee, A. A., Vella, D. & Wettlaufer, J. S. Fluctuation spectra and force generation in nonequilibrium systems. *Proc. Natl Acad. Sci. USA* **114**, 9255–9260 (2017).

48. Parsegian, V. A. *Van der Waals Forces* (Cambridge Univ. Press, 2006).

49. Israelachvili, J. N. *Intermolecular and Surface Forces* (Academic, 2011).

50. Chen, S. et al. Rapid seedless synthesis of gold nanoplates with microscaled edge length in a high yield and their application in SERS. *Nanomicro Lett.* **8**, 328–335 (2016).

51. Mitamura, K., Imae, T., Saito, N. & Takai, O. Fabrication and self-assembly of hydrophobic gold nanorods. *J. Phys. Chem. B* **111**, 8891–8898 (2007).

52. Notsu, H., Kubo, W., Shitanda, I. & Tatsuma, T. Super-hydrophobic/super-hydrophilic patterning of gold surfaces by photocatalytic lithography. *J. Mater. Chem.* **15**, 1523–1527 (2005).

53. Magazzú, A. et al. Controlling the dynamics of colloidal particles by critical Casimir forces. *Soft Matter* **15**, 2152–2162 (2019).

54. Lin, B., Yu, J. & Rice, S. A. Direct measurements of constrained Brownian motion of an isolated sphere between two walls. *Phys. Rev. E* **62**, 3909–3919 (2000).

55. Dufresne, E. R., Altman, D. & Grier, D. G. Brownian dynamics of a sphere between parallel walls. *Europhys. Lett.* **53**, 264 (2001).

56. Happel, J. & Brenner, H. *Low Reynolds Number Hydrodynamics: with Special Applications to Particulate Media* (Martinus Nijhoff, 2012).

57. Garcia-Sanchez, D., Fong, K. Y., Bhaskaran, H., Lamoreaux, S. & Tang, H. X. Casimir force and in situ surface potential measurements on nanomembranes. *Phys. Rev. Lett.* **109**, 027202 (2012).

58. Soyka, F., Zvyagolskaya, O., Hertlein, C., Helden, L. & Bechinger, C. Critical Casimir forces in colloidal suspensions on chemically patterned surfaces. *Phys. Rev. Lett.* **101**, 208301 (2008).

59. Tröndle, M. et al. Trapping colloids near chemical stripes via critical Casimir forces. *Mol. Phys.* **109**, 1169–1185 (2011).

Methods

Calculation of the Casimir–Lifshitz and critical Casimir forces

The theoretical model which relates the measured experimental temperatures to the equilibrium heights of the flake in the presence of two different boundary conditions of the order parameter accounts for the following forces: the weight and buoyancy of the flake, the DLVO electrostatic interaction, the Casimir–Lifshitz force and the critical Casimir force.

Weight and buoyancy. For the hexagonal flakes used in our experiments (Fig. 2a), the sum of the weight and the buoyancy is within the range of 5–30 fN, depending on the volume of the flake. In the case of a flake suspended above a gold-coated substrate, this sum is negligible in comparison with the Casimir–Lifshitz attraction and the electrostatic forces, the magnitude of which is within the range of ~1–10 pN for distances on the order of ~100–200 nm, such as those observed in our experiments. In the case of a flake suspended above an uncoated silica substrate, instead, the sum of the weight and buoyancy is not negligible compared with the other relevant forces because the flake hovers at a higher h and the Casimir–Lifshitz attraction is ~20 times smaller (for the same h). Hence, we included weight and buoyancy in all the theoretical modelling, although omitting their contribution for the gold-coated substrate does not change the results for the explored experimental parameters.

Electrostatic force. The DLVO electrostatic force[49] F_{ES} between the flake and the substrate, at a distance h, is modelled according to Eq. (3) and is parametrized by the Debye screening length of the critical mixture λ_D and the parameter with dimensions of pressure, P_0. For each choice of the surfaces involved, we fitted these parameters independently, determining the combination of values of λ_D and P_0 that minimizes the χ^2 (square error) when comparing the experimental data for the average height $\langle h \rangle$ with the model. As a result, the various substrates turn out to be characterized by slightly different values of the parameters of the electrostatics, with a pronounced difference in the case of an uncoated surface, where the existence of larger separations between the flake and the substrate leads to larger fluctuations of $\langle h \rangle$ (Extended Data Fig. 4). For our experiments, we found the following combinations:

gold-coated $(-,-)$	$\lambda_D = 16 \pm 0.5\,\mathrm{nm}$	$P_0 = 3.7 \pm 0.6\,\mathrm{kPa}$
gold-coated $(+,-)$	$\lambda_D = 17 \pm 0.5\,\mathrm{nm}$	$P_0 = 1.5 \pm 0.3\,\mathrm{kPa}$
uncoated silica $(-,-)$	$\lambda_D = 17 \pm 0.5\,\mathrm{nm}$	$P_0 = 28 \pm 5\,\mathrm{kPa}$

As expected, these three independent fits give very similar values of λ_D, while the value of P_0 in the case of uncoated silica is much larger than in the case of the gold-coated substrate, indicating a stronger electrostatic repulsion.

Casimir–Lifshitz force. The Casimir–Lifshitz force F_{CL} in Eq. (1) was calculated according to ref. [48] for the layered planar bodies involved in the experimental setup in Fig. 1a. The corresponding free energy per unit area is given by

$$G_{CL}(h) = -\frac{A_{2/3}(h)}{12\pi h^2} - \frac{A_{1/3}(h+a_1)}{12\pi(h+a_1)^2} - \frac{A_{2/4}(h+b)}{12\pi(h+b)^2} - \frac{A_{1/4}(h+a_1+b)}{12\pi(h+a_1+b)^2}, \quad (5)$$

where $A_{2/3}, A_{1/3}, A_{2/4}$ and $A_{1/4}$ are the Hamaker functions (Supplementary Information Section I), a_1 is the thickness of the gold layer deposited on the substrate and b is the thickness of the gold flake. In the simpler case of a bottom slide of uncoated silica, instead, the dispersion forces can be derived from

$$G_{CL}(h) = -\frac{A_{5/3}(h)}{12\pi h^2} - \frac{A_{5/4}(h+b)}{12\pi(h+b)^2}, \quad (6)$$

where $A_{5/3}$ and $A_{5/4}$ are the corresponding Hamaker functions (Supplementary Information Section I). Note that, in this analysis, we neglect any spatial inhomogeneities within the fluid, which are known to generate an additional effective interface potential scaling as $1/h^3$ (ref. [60]).

Critical Casimir force. The expression for the critical Casimir force F_{crit} in Eq. (2) depends on the correlation length ξ of the order parameter fluctuation of the binary liquid mixture, which is related to $\Delta T < 0$ as $\xi = \xi_0(|\Delta T|/T_c)^{-\nu}$, where $\xi_0 \approx 0.22\,\mathrm{nm}$ for the water–2,6-lutidine mixture while $\nu \simeq 0.63$ is the critical exponent of the Ising universality class to which the mixture belongs[30].

Total force and potential. The total force F_{tot} acting on a flake is

$$F_{tot}(h, \Delta T) = F_{ES}(h) + F_{CL}(h) + F_{crit}(h, \Delta T) + F_{w+b}, \quad (7)$$

where the term F_{w+b} due to weight and buoyancy can be neglected in the case of a flake suspended on a gold-coated substrate at the typical distances observed in our experiments, as explained above. The total potential U_{tot} of the flake is therefore

$$U_{tot}(h, \Delta T) = U_{ES}(h) + G_{CL}(h)S + U_{crit}(h, \Delta T) + U_{w+b}, \quad (8)$$

in terms of the potentials corresponding to the forces shown in Eq. (7). In the case of a gold flake floating on a gold-coated substrate, $U_{tot}(h, \Delta T)$ displays a very sharp minimum at a certain $h(\Delta T)$ for all ΔT, while for the flake suspended on an uncoated silica substrate, the minimum of the potential becomes shallow for $|\Delta T| \gtrsim 0.1\,\mathrm{K}$.

When comparing with experiments, one has to keep in mind that the experimentally accessible quantity is the average height of the potential

$$\langle h \rangle = \int_0^{+\infty} dh\, h\, P(h, \Delta T), \quad (9)$$

which is defined in terms of the equilibrium probability distribution function $P(h, \Delta T)$ associated with the potential $U_{tot}(h, \Delta T)$, that is,

$$P(h, \Delta T) = \frac{1}{Z} e^{-\frac{U_{tot}(h,\Delta T)}{k_B T}}, \quad (10)$$

where $Z = \int_0^{+\infty} e^{-\frac{U_{tot}(h,\Delta T)}{k_B T}}\, dh$ Hence, the comparison with the experimental data must consider the equilibrium height of the potential h, defined as

$$\frac{dU_{tot}(h_{eq})}{dh} = 0. \quad (11)$$

In a potential with a sharp dip, h_{eq} and $\langle h \rangle$ are often very close, and therefore $\langle h \rangle$ can be estimated by h_{eq}. In contrast, in a shallow, asymmetric potential, the equilibrium height h may differ substantially from the average height $\langle h \rangle$. In the experimental conditions considered here, the difference between $\langle h \rangle$ and h_{eq} for a gold flake suspended on an uncoated silica surface is $|\langle h \rangle - h_{eq}| \approx 50$–$100\,\mathrm{nm}$, while when the flake is suspended on a gold substrate, this difference is $<5\,\mathrm{nm}$.

To compare the predictions of the model discussed above with the experimental data, we focus on the average height $\langle h \rangle$ due to the total potential, considering also the amplitude Δh of its fluctuations. In our calculation and fitting procedure, Δh is set to correspond to a confidence level of 68%. Only $F_{crit}(h)$ and $U_{crit}(h)$ depend strongly on the minute variations of ΔT (via the dependence on $\xi(\Delta T)$ of the scaling function $\theta(h/\xi)$ in Eq. (2)). The electrostatic and Casimir–Lifshitz interactions do not depend on ΔT, with the caveat that, when the correlation length ξ of the solvent becomes comparable to the Debye screening length λ_D of the electrostatics, other effects might come into play.

In fact, when λ_D becomes comparable to ξ, the description of the electrostatics with Eq. (3) is no longer appropriate. Given that the estimated value of the Debye screening length is $\lambda_D \simeq 16$–17 nm, the value of the corresponding correlation length ξ is smaller than λ_D for the typical temperature differences in our system up to $\Delta T \approx -0.1$ K.

We first determined the parameters of the electrostatic interaction by fitting the value of the Debye screening length λ_D and the prefactor P_0 such that they minimize

$$\chi^2 = \sum_{j=1}^{N} \frac{\left(\langle h_{j,\text{exp}}\rangle - \langle h_j\rangle\right)^2}{\Delta h_j^2}, \tag{12}$$

where $\langle h_j\rangle$ and Δh_j were calculated for each different combination of parameters for the experimental temperature ΔT_j of the experimental data $\langle h_{j,\text{exp}}\rangle$. The fitted λ_D is in the range of values obtained in similar experiments[32,53].

Experimental details

We consider a dilute suspension of gold flakes (monocrystalline, polydisperse and with average thickness $d = 34 \pm 10$ nm determined via atomic force microscopy measurements[23]). The gold nanoflakes are wet-chemically synthesized using a rapid and seedless method in aqueous solution described in detail in ref. [50]. Briefly, 100 µL of 100 mM HAuCl$_4$ was added to 3 mL of 20 mM CTAB aqueous solution in a glass vial, and the mixture was gently mixed and left undisturbed for several minutes. Then, 100 µL of 100 mM ascorbic acid was added to the mixture, followed by rapid inversions of the vial for 10 s. The resulting solution was immediately placed in a water bath at 85 °C and kept undisturbed for about 1 h. The products were washed by centrifugation at 4,000 rpm (2,218g) for 10 min and finally dispersed in deionized water for further experiments.

The flakes obtained as described above were then suspended in a near-critical binary liquid mixture of water and 2,6-lutidine at the critical composition of lutidine $c_L^c = 0.286$, having a lower critical point at $T_c \approx 34$ °C (ref. [61] and Extended Data Fig. 8). The suspension was confined in a sample cell between a microscopy slide and a cover slip spaced by about 300 µm.

On top of the cover slip, a 40-nm-thick gold layer was sputtered homogeneously across the sample. The cover slip was then left overnight in 1 mM solution of thiols (1-octanethiol for hydrophobic and 6-mercapto-1-hexanol for hydrophilic treatment) and ethanol, creating a SAM on top of the gold. To create a hydrophobic SAM on top of the glass, trichloro(1H,1H,2H,2H-perfluorooctyl)silane was evaporated for 4 h under vacuum. The stark contrast in the resulting wetting angle between hydrophilic SAM ($\theta = 19°$, measured from the side) and hydrophobic SAM ($\theta = 102°$) of a 10 µL water droplet can be seen in Extended Data Fig. 9.

For the patterned substrate shown in Fig. 4, an additional 3-nm-thick layer of titanium was added to the glass substrate for better adhesion before sputtering gold. The patterned gold stripes were fabricated by direct laser writing and lift-off. The substrates were spin coated with LOR 3A (4,000 rpm for 60 s, baking at 200 °C for 5 min) and S1805 (3,000 rpm for 45 s, baking at 110 °C for 1 min). The samples were exposed using a Heidelberg DWL2000 direct laser writer and developed in MF CD26 for 50 s. Titanium and gold were deposited, and lift-off was performed in hot remover 1165 at 70 °C overnight.

A schematic of the experimental setup is shown in Extended Data Fig. 2. The whole sample is temperature stabilized by using a two-stage temperature controller consisting of a copper-plate heat exchanger coupled to a circulating water bath at $T_0 = 32.5$ °C (T100, Grant Instruments) and two Peltier elements (TEC3-6, Thorlabs) attached to the imaging objective and in feedback with a controller unit (TED4015, Thorlabs), reaching ±20 mK temperature stability[32,53]. The flake's translational motion is captured using digital video microscopy at a frame rate of 100 Hz. The particle images are thresholded to determine the particle's centroid. The reconstructed trajectory is then analysed using standard methods.

Diffusion of a flake

The determination of the equilibrium height h of a flake depends on three crucial factors: the measurement of the diffusion constant D, the hydrodynamic simulations for extracting h from D and the presence of spurious concentrations of salt in solution, as discussed below. In principle, the diffusion constant D depends on the flake diffusion in three spatial dimensions. However, as the flake has a mass density of $\rho_{Au} \approx 17 \times 10^3$ kg m^{-3}, much larger than that of the surrounding fluid ($\rho_{WL} \approx 0.98 \times 10^3$ kg m^{-3}), it settles quickly from bulk into proximity of the substrate at an equilibrium distance h so that, in practice, we observe its motion along the horizontal x–y plane only, whereas any motion along the vertical direction z is negligible. A theoretical estimate based on the potential we obtain with our model (Eq. (8)) gives that a typical amplitude of the vertical fluctuation Δh is within $\Delta h \lesssim 5$ nm.

The presence of salts in solution, which further screen the flake, might reduce the repulsive electrostatic forces and therefore its heights above the surface, as studied previously[23]. However, we can neglect any influence of salt in our system, as our gold flakes, originally prepared in CTAB buffer solution, have been diluted more than 2,000 times with deionized water. This is confirmed by the fact that, even after the surface treatment with SAM or in control experiments in pure water, the average height $h \approx 100$ nm of the flake does not change (Extended Data Fig. 4).

Hydrodynamic simulations

In our hydrodynamics simulations, a flake is modelled as a rigid assembly of N spheres (typically, $N \approx 1,000$–$3,000$) of radius r, with $r = b/2$, where b is the thickness of the flake, glued together and arranged on a regular hexagon. The assembled object is immersed in an incompressible Newtonian fluid bounded by a no-slip wall. At low Reynolds numbers, the fluid dynamics is governed by the Stokes equations, in which viscous forces dominate inertial forces. Under these conditions, the translational velocity $\mathbf{V}_i$ of the sphere labelled by the index $i = 1, ..., N$ and composing the conglomerate is linearly related to the force $\mathbf{F}_j$ exerted on either the same sphere ($j = i$) or on adjacent spheres via the hydrodynamic mobility tensor[62]. Specifically,

$$\mathbf{V}_i = \mu^S \mathbf{F}_i + \sum_{j \neq i} \mu^P \mathbf{F}_j, \tag{13}$$

where μ^S denotes the self-mobility tensor of a single sphere sedimenting near a hard wall and μ^P corresponds to the pair mobility tensor quantifying the hydrodynamic interactions between the spheres and the wall[63]. Here we employ the well-established Rotne–Prager approximation[64] combined with the Blake solution[65] to account for the corrections due to the presence of the wall. The diffusion coefficient is obtained from the drag coefficient, which, in turn, is obtained by following the usual procedure of evaluating the mean drag per sphere within the assembly. The accuracy of our approach has been assessed by close comparison of the predicted bulk drag coefficients with the exact numerical simulations of a closely packed conglomerate of spheres, which was obtained by using the freely available and open-source library HYDROLIB (Extended Data Fig. 10).

These results allow us to simulate the diffusion of a regular hexagonal flake with side length a at height h above a wall as in the representative case of a flake with $a = 840$ nm in Fig. 2d (cases of particles with different sizes are shown in Extended Data Fig. 10c).

Moreover, hydrodynamic simulations allow us to investigate the influence of a possible Brownian rotation on the diffusion of the flake in the presence of the confining interface, which we find to be negligible.

As a last remark about the hydrodynamic simulation, its underlying assumption is that the viscosity of the solvent does not depend substantially on temperature. This is actually the case in experiments. In fact, the viscosity of water–lutidine at critical concentration does not change appreciably in the temperature range of our experiments. Moreover, we do not possess experimental evidence of the presence of a wetting layer.

Optical measurements and analysis

Reflection spectra at normal incidence (numerical aperture 0.5) were collected by using an inverted microscope (Nikon Eclipse TE2000-E) equipped with an oil-immersion 100× objective (switchable numerical aperture of 0.5–1.3, Nikon), directed to a fibre-coupled spectrometer (Andor Shamrock SR-303i), equipped with a Andor iDus 420 charge-coupled detector (see schematic in ref. [23]). The obtained reflection spectra were analysed by the standard transfer matrix method[23].

Data availability

All experimental data are available via the depository figshare under https://doi.org/10.6084/m9.figshare.20037581.v1[66]. Source data are provided with this paper.

Code availability

The codes that support the findings of this study are available from the corresponding authors upon reasonable request.

References

60. Dietrich, S. & Napiórkowski, M. Analytic results for wetting transitions in the presence of van der Waals tails. *Phys. Rev. A* **43**, 1861–1885 (1991).
61. Grattoni, C. A., Dawe, R. A., Seah, C. Y. & Gray, J. D. Lower critical solution coexistence curve and physical properties (density, viscosity, surface tension, and interfacial tension) of 2,6-lutidine + water. *J. Chem. Eng. Data* **38**, 516 (1993).
62. Kim, S. & Karrila, S. J. *Microhydrodynamics: Principles and Selected Applications* (Courier Corporation, 2013).
63. Swan, J. W. & Brady, J. F. Simulation of hydrodynamically interacting particles near a no-slip boundary. *Phys. Fluids* **19**, 113306 (2007).
64. Rotne, J. & Prager, S. Variational treatment of hydrodynamic interaction in polymers. *J. Chem. Phys.* **50**, 4831–4837 (1969).
65. Blake, J. R. A note on the image system for a Stokeslet in a no-slip boundary. *Math. Proc. Camb. Philos. Soc.* **70**, 303–310 (1971).
66. Schmidt, F. et al. Tunable critical Casimir forces counteract Casimir–Lifshitz attraction. *Figshare* https://figshare.com/articles/media/Tunable_critical_Casimir_forces_counteract_Casimir_Lifshitz_attraction/20037581 (2022).

Author contributions

All authors discussed the results and wrote or edited the manuscript. F.S., B.M. and G.V. planned the experiments. F.S. and B.M. performed the experiments. A.D.-M.-I. and H.L. conducted the hydrodynamic simulations. A.C. and A.G. conceptualized the theoretical model and performed the force simulations. F.S. and R.V. fabricated the experimental samples. B.M. fabricated the flakes.

Competing interests

The authors declare no competing interests.

Additional information

Extended data is available for this paper at https://doi.org/10.1038/s41567-022-01795-6.

Supplementary information The online version contains supplementary material available at https://doi.org/10.1038/s41567-022-01795-6.

Correspondence and requests for materials should be addressed to Falko Schmidt or Giovanni Volpe.

Peer review information *Nature Physics* thanks the anonymous reviewers for their contribution to the peer review of this work

Reprints and permissions information is available at www.nature.com/reprints.
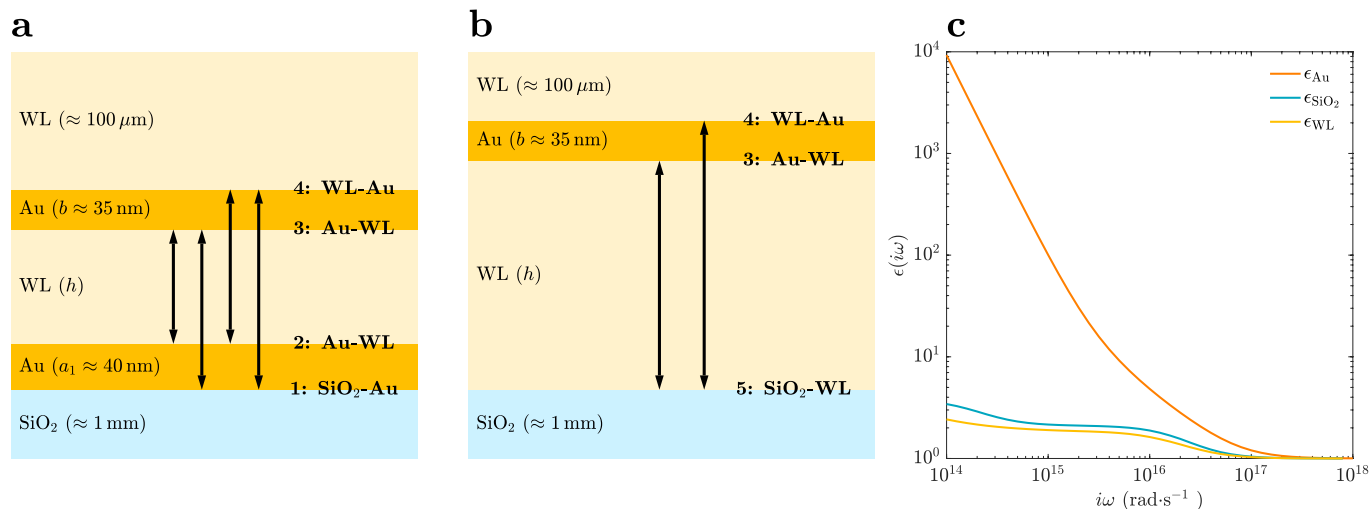
**Extended Data Fig. 1 | Schematics of the materials involved in the experiments. a**, Configuration used to calculate the force acting on the flake depending on the material properties and on the distances indicated by the arrows. See Eqs. (1), (S1), and (S2) for the case of a gold-coated silica substrate. WL indicates the water–2,6-lutidine mixture, SiO$_2$ the silica, and Au the gold layers. **b**, Same as panel **a** but for the case of an uncoated silica substrate. In both panels, the text indicates each interface in the notation used for the Hamaker function (Eqs. (S1) and (S3)) and the $\Delta_{a\text{-}b}$ (Eq. (S2)). The order of the symbols a and b in the subscript of $\Delta_{a\text{-}b}$ follows the convention to determine the Casimir–Lifshitz force contribution defined in ref. [48], that is, the symbol that comes first always refers to the material that is on the outside of the interface looking toward the separating medium, which in our case is the layer of water–2,6-lutidine of thickness h. The double arrows in both panels indicate the pair of interfaces considered for each Hamaker function: in **a** the terms in Eqs. (S1); in **b** the terms in Eqs. (S3). **c**, Dielectric response functions of the materials involved in the experiment. For the parametrization of these functions with respect to water–2,6-lutidine and silica we follow ref. [30], while for gold we follow ref. [48], page 268, Table L2.4. Gold, Four-term fit to absorption data.
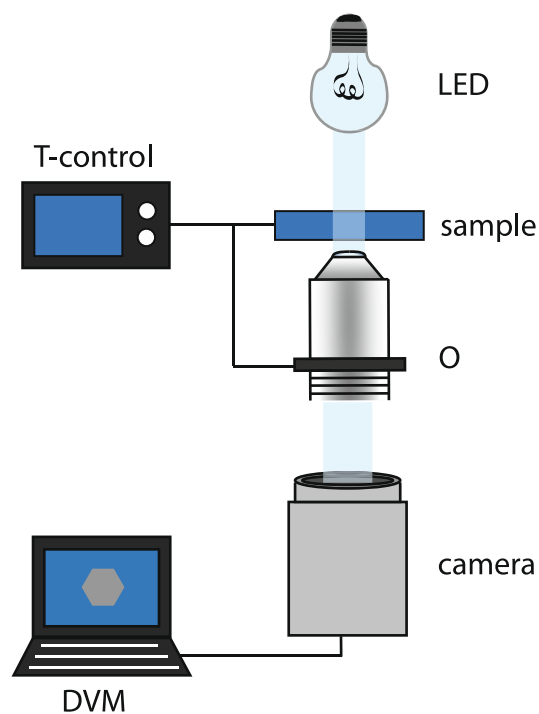
Extended Data Fig. 2 | Schematic of the experimental setup for digital video microscopy. Homemade version of an inverted brightfield microscope consisting of a white light (LED) illuminating the sample from above, which is temperature-stabilized by using a two-stage temperature controller at the sample and by indirect heating of the objective (O). The scattered light is collected by the 100 × objective (numerical aperture = 1.30) and projected onto a camera. The flake motion is tracked and analysed with digital video microscopy.
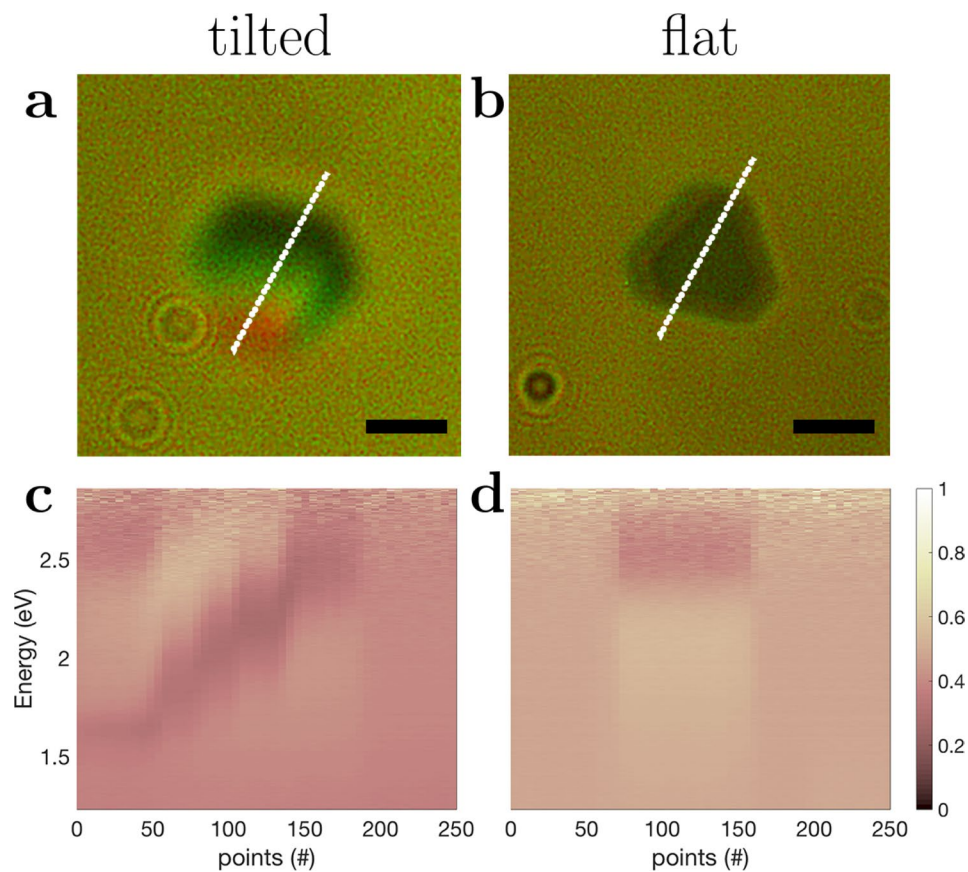
Extended Data Fig. 3 | Height measurement of a metal flake using Fabry–Pérot cavity modes. a, In a bright-field image of a gold flake, the tilt with respect to the substrate becomes visible as a change in colour, whereas in **b**, no colour variation is observed for a flake oriented parallel to the substrate. **c**, The Fabry–Pérot cavity modes are measured across the flake along the dashed lines indicated in panels **a** and **b** and reveal a shift in energy corresponding to a variation of the distance h from the sub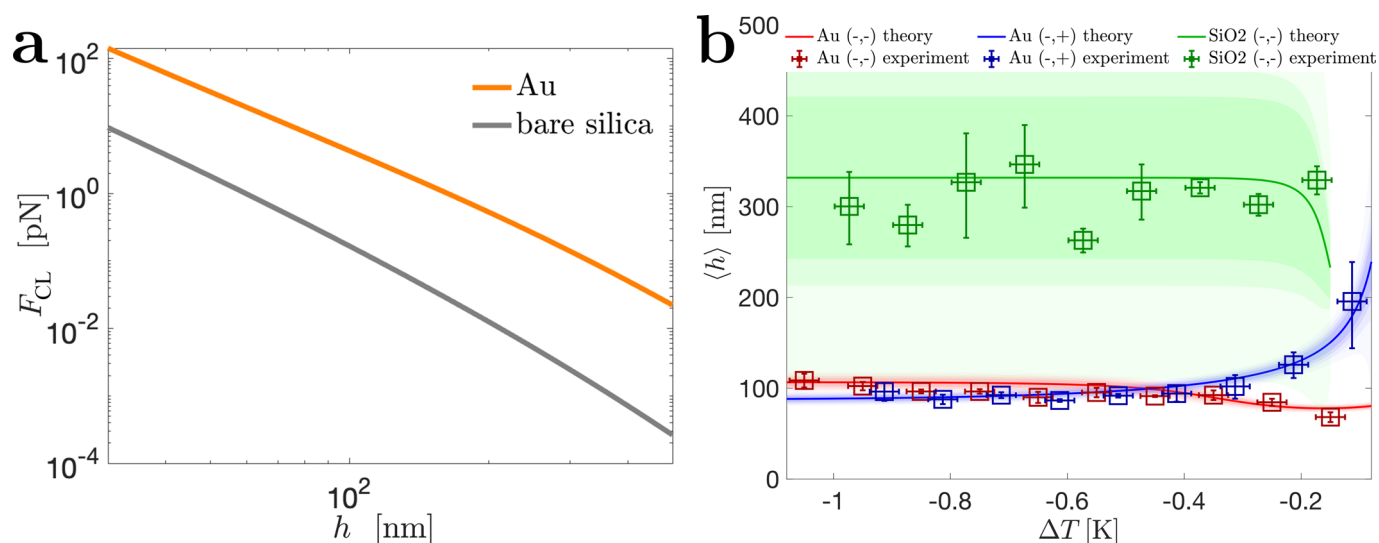strate from $h = 90 \pm 10$ to 210 ± 10 nm. In panel **d**, instead, the measured energy values remain constant and correspond to a distance $h = 90 \pm 10$ nm above the substrate. The colour bar shows the measured reflection intensity. Scale bars in panels **a** and **b** correspond to 1 μm. The analysis of the Fabry–Pérot experimental data and the determination of the local height of the cavity has been conducted according to the transfer-matrix model, which is described in ref. [23].
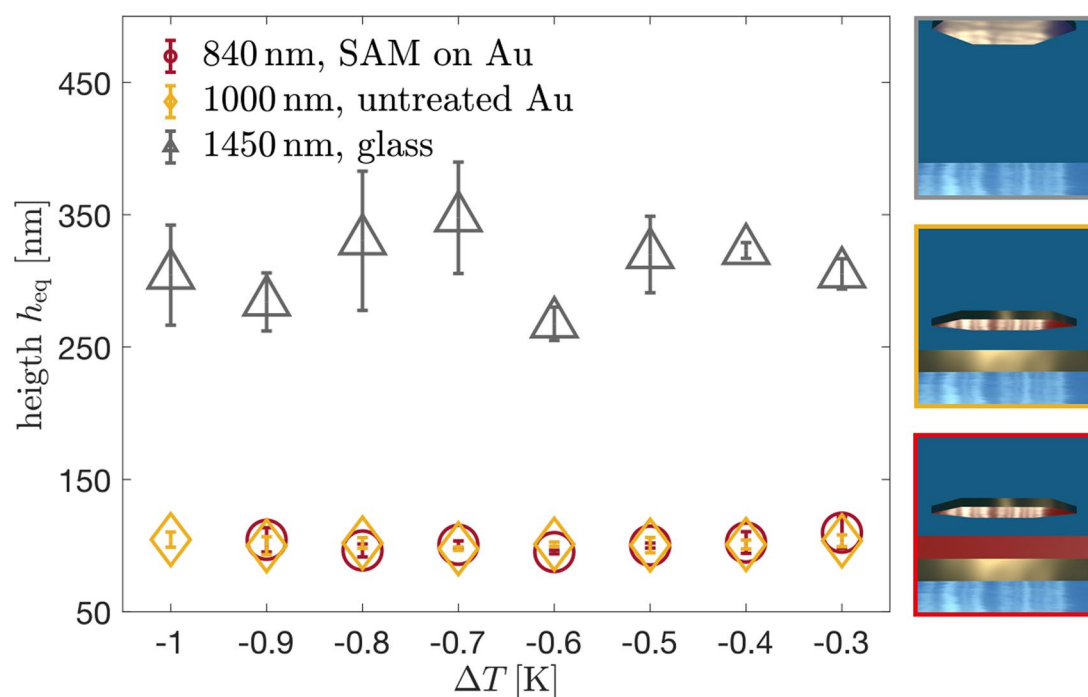
Extended Data Fig. 4 | Dependence of the flake height on surface treatment. Far away from T_c, the particle height h above a gold surface is reduced to $h \approx 100$ nm due to the attractive Casimir–Lifshitz force, independent of whether a SAM is present (red circles, inset with red frame) or not (yellow diamonds, inset with yellow frame). For dielectric surfaces such as silica (grey triangles, inset grey frame), the particle fluctuates at a much larger distance $h \approx 300$ nm because of the substantially smaller attractive Casimir–Lifshitz force. Here, all measurements have been performed far away from criticality with $\Delta T \leq -0.3$ K, in a range where these results are independent of ΔT. All error bars indicated in the plot correspond to the standard deviation and amount to about 5% of the absolute value. The data are presented as mean values.

a, Casimir–Lifshitz force acting on a gold flake suspended at a height h above a gold coated substrate (orange line) or an untreated silica substrate (grey line).

**Extended Data Fig. 5 | Comparison between the dispersion forces on a flake suspended on an untreated silica substrate and on a gold-coated substrate. a**, Casimir–Lifshitz force acting on a gold flake suspended at a height h above a gold coated substrate (orange line) or an untreated silica substrate (grey line). The magnitude of the force is represented in a log-log plot and is calculated for a reference hexagonal flake with side length equal to 700 nm. The force is attractive for both substrates, but in the case of an untreated silica substrate the force is one order of magnitude smaller than in the gold-coated case. **b**, Experimental values of ⟨*h*⟩ (see Eq. (9) for its definition) of the flake for the various cases, that is, gold flake suspended on a gold-coated substrate with hydrophilic SAM (red symbols), hydrophobic SAM (blue symbols), and uncoated silica substrate (green symbols). The solid lines represent the theoretical model. The resulting fit is in good agreement with the experimental measurements for all

substrates. It is worth noting that the confidence interval for the values of ⟨*h*⟩ for the uncoated silica substrate are much larger than those for the gold-coated substrates. This happens as the minimum of the total potential is very shallow for an uncoated silica substrate, because the Casimir–Lifshitz forces are much weaker in this case. At $T \ll T_c$, that is, in the absence of attractive critical Casimir forces, the gravity plus buoyancy is the only force that is effective in pushing the flake towards the substrate. In the case of a gold-coated substrate, the Casimir–Lifshitz forces are very relevant for $T \ll T_c$, and the resulting total potential has a very pronounced minimum, which is reflected in the very narrow error intervals. In the figure, the darker shade of each colour represents the 68% confidence interval. The error on the experimental data is the standard deviation from the mean of three measurements. The data are presented as mean values.
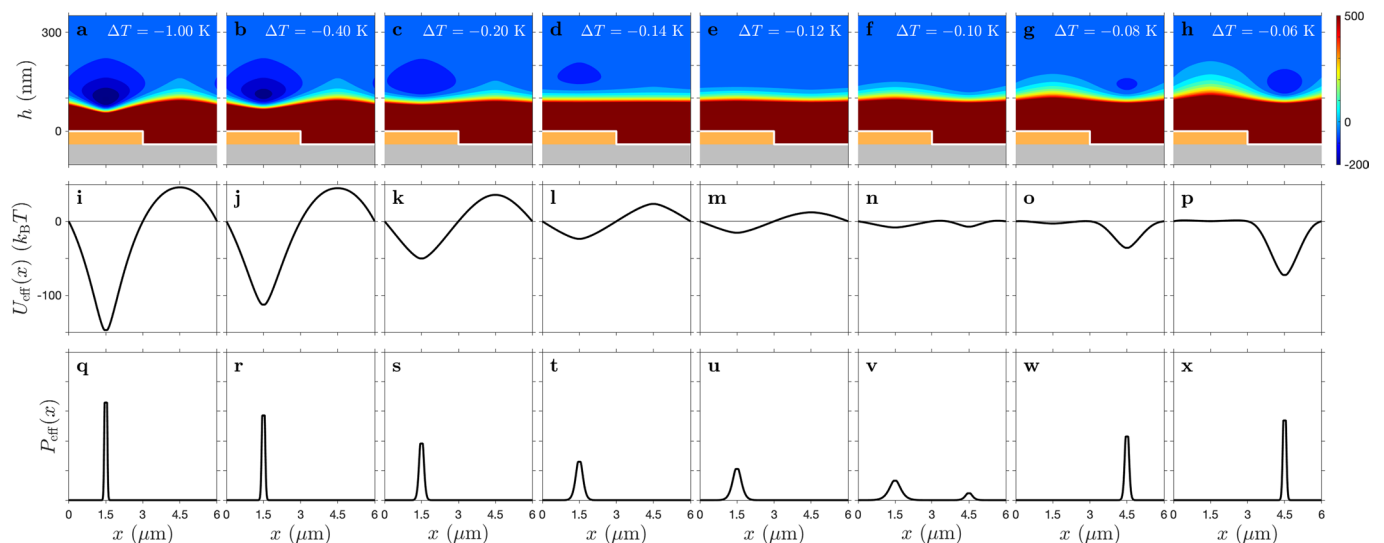
Extended Data Fig. 6 | Trapping and release of a flake, prediction of the theoretical model. a–h, Two dimensional potential $U_{tot}(\Delta T; h, x)$, **i–p**, effective lateral potential $U_{eff}(\Delta T; x)$, and **q–x**, effective lateral probability distribution function $P_{eff}(\Delta T; x)$ for a disk-like flake (radius $a = 1450$ nm, thickness $b = 40$ nm) hovering on a patterned substrate with hydrophobic, 3-μm-wide, gold-coated stripes alternating periodically with hydrophilic, 3-μm-wide, uncoated silica stripes. The thickness of each gold-coated stripe is $a_1 = 30$nm. As shown in panels **a–h**, the height of the flake h on the surface is measured with respect to the upper surface of the gold stripes; hence, when considering the height of the flake with respect to the hydrophilic uncoated surface, one must take into account the additional term a_1. The profile of the substrate is represented in panels **a–h**. The value of the two-dimensional total potential is represented with a contour plot. For $\Delta T = -1$ K, the minimum of the total potential is located over the gold-coated stripe at its centre (for symmetry reasons) about 100nm above the surface. Upon increasing the temperature towards T_c, the minimum

of the potential becomes less and less deep, and for $\Delta T > -0.1$ K, the minimum is located above the uncoated silica stripe. In **i–p**, the effective lateral potential $U_{eff}(\Delta T; x)$ defined in Eq. (S8) is represented with a black continuous line. The zero of the potential is set at $x = 0$. For $\Delta T \leq -0.12$K (**i–m**), the effective potential has a single minimum at $x = 1.5\mu$m; for $\Delta T \geq -0.1$K (**o,p**), the effective potential has a single minimum at $x = 4.5\mu$m, that is, localized at the centre of the uncoated silica stripe; for $\Delta T = -0.1$K (**n**), the effective potential has two local minima. In **i–p** the effective probability distribution $P_{eff}(\Delta T; x)$ defined in Eq. (S9) is represented with a black continuous line. In **i–m**, $P_{eff}(\Delta T; x)$ has a single peak at $x = 1.5\mu$m, indicating that the flake is localized on the gold stripe. The peak is initially very sharp, but becomes broader and less high upon increasing the temperature towards T_c. In **n**, $P_{eff}(\Delta T; x)$ has two peaks. In **n,o**, the peak is again one, this time localized at the centre of the uncoated silica stripe. In this model, the parameters for the electrostatic interaction are $\lambda_D = 17$ nm and $P_0 = 1.5$ kPa for the gold-coated stripes, whereas $P_0 = 28.8$ kPa for the gold-coated stripes.
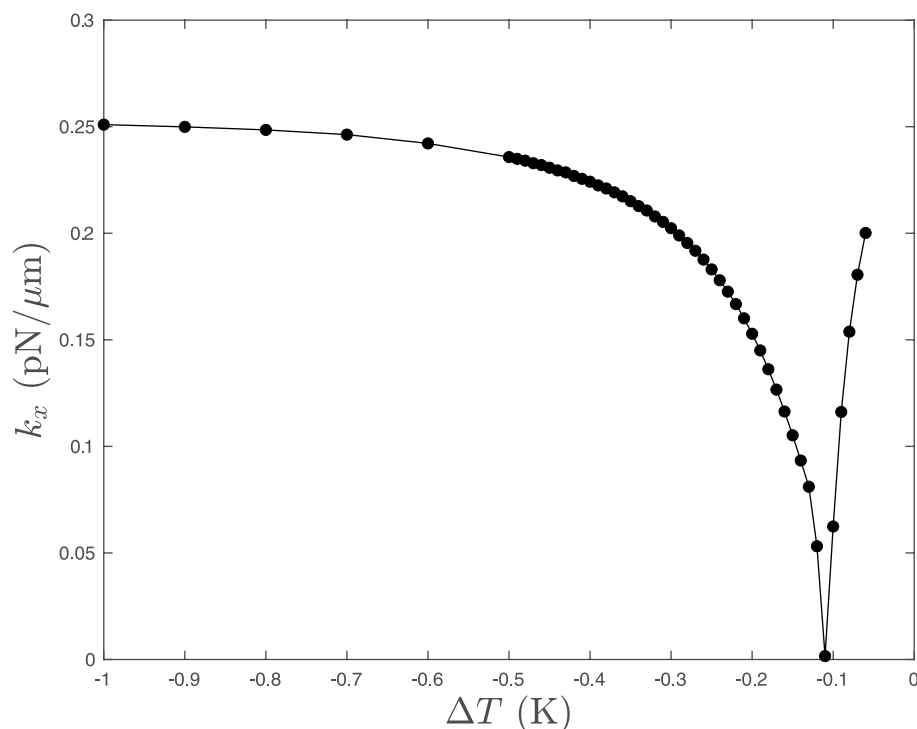
Extended Data Fig. 7 | Effective stiffness predicted by the theoretical model.
Stiffness of the lateral trapping (k_x) calculated for the effective potential U_{eff} as a function of $\Delta T = T - T_c$. Here we calculate k_x using the variance of the peak of the probability distribution $P_{\text{eff}}(\Delta T; x)$, that is, $k_x = \frac{k_B T}{\sigma^2}$ where $\sigma^2 = \int_{x_1}^{x_2} P_{\text{eff}}(\Delta T; x) \left(x - x_{\text{peak}}\right)^2 \mathrm{d}x$. The extrema of the integral are defined as $x_1 = 0, x_2 = 3\,\mu$m for the ΔTs where the absolute peak of $P_{\text{eff}}(\Delta T; x)$ falls in the centre of the gold-coated stripe, and as $x_1 = 3\,\mu$m, $x_2 = 6\,\mu$m for the ΔTs where the absolute peak of $P_{\text{eff}}(\Delta T; x)$ falls in the centre of the uncoated silica stripe. We

remark that, for our model, σ is determined not only by the parameters of the interaction, but also by the geometrical characteristics of the system. In particular, the main factor affecting σ in our model is the difference between the diameter of the flake and the width of the stripes. In fact, $U_{\text{eff}}(\Delta T; x)$ is necessarily flat over an interval of length $w - 2R$, where w is the thickness of the stripe and R is the radius of the disk-like flake. Hence, for the same parameters describing the interaction per unit area, different flake dimensions have a σ that is at least $w/2 - R$, which increases upon decreasing R.
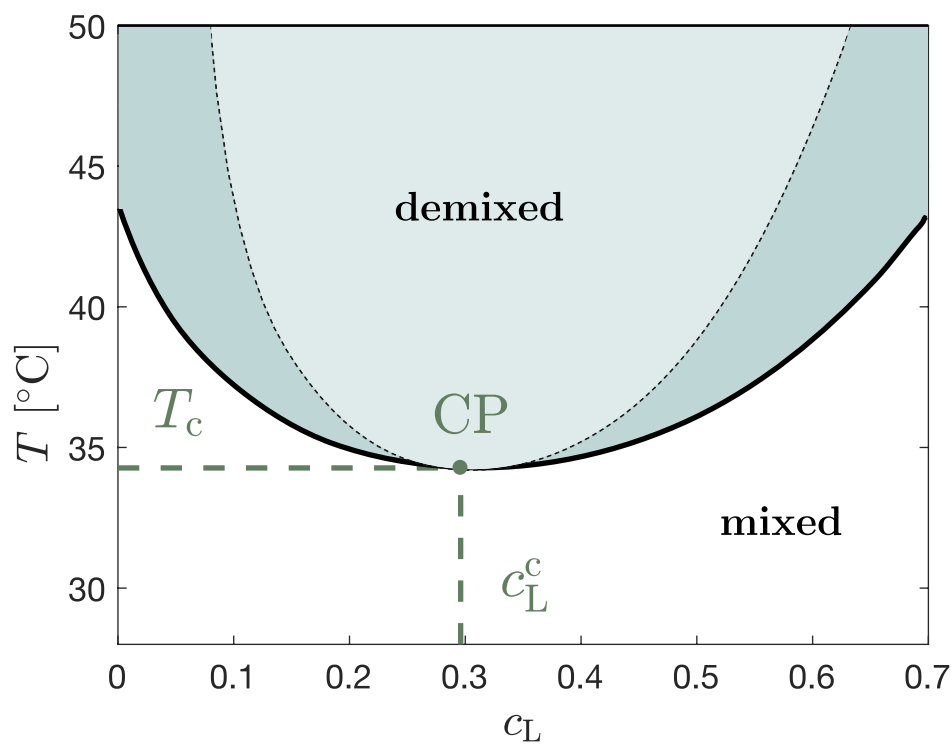
Extended Data Fig. 8 | Phase diagram of a water–2,6-lutidine liquid mixture. The binary solution of water and 2,6-lutidine possesses two distinct phases given by the binodal (black line) and spinodal line (black dotted line) separating mixed from demixed phases. The solution is prepared at $T_0 = 32.5$ °C and the critical concentration of 2,6-lutidine $c_L^c = 0.286$ near the critical point (CP) with $T_c \approx 34$ °C. The data are obtained from ref. [61].
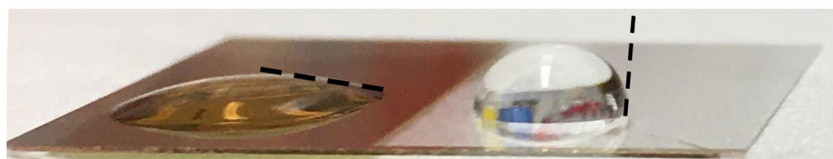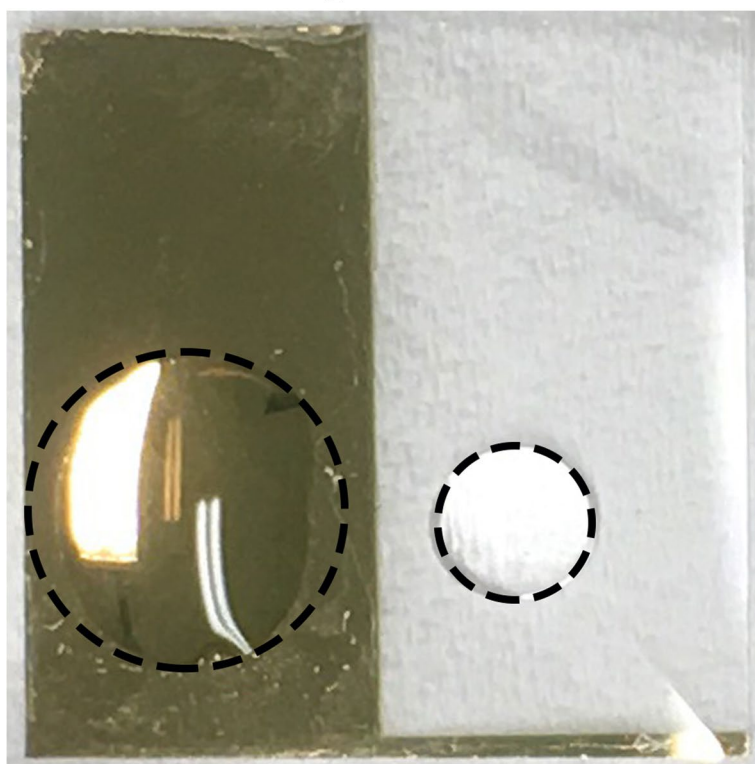
**Extended Data Fig. 9 | Effect of the treatment with different self-assembled monolayers (SAM).** Side and top view of a cover glass slide half of which has been sputtered with a 30 nm gold layer (left half). The treatment with hydrophilic thiols attached to gold and hydrophobic silanation to glass is visible by the difference of the wetting angle (black dashed line in the side view) and by the spreading (black dashed circle in the top view) of a 10 μL droplet.
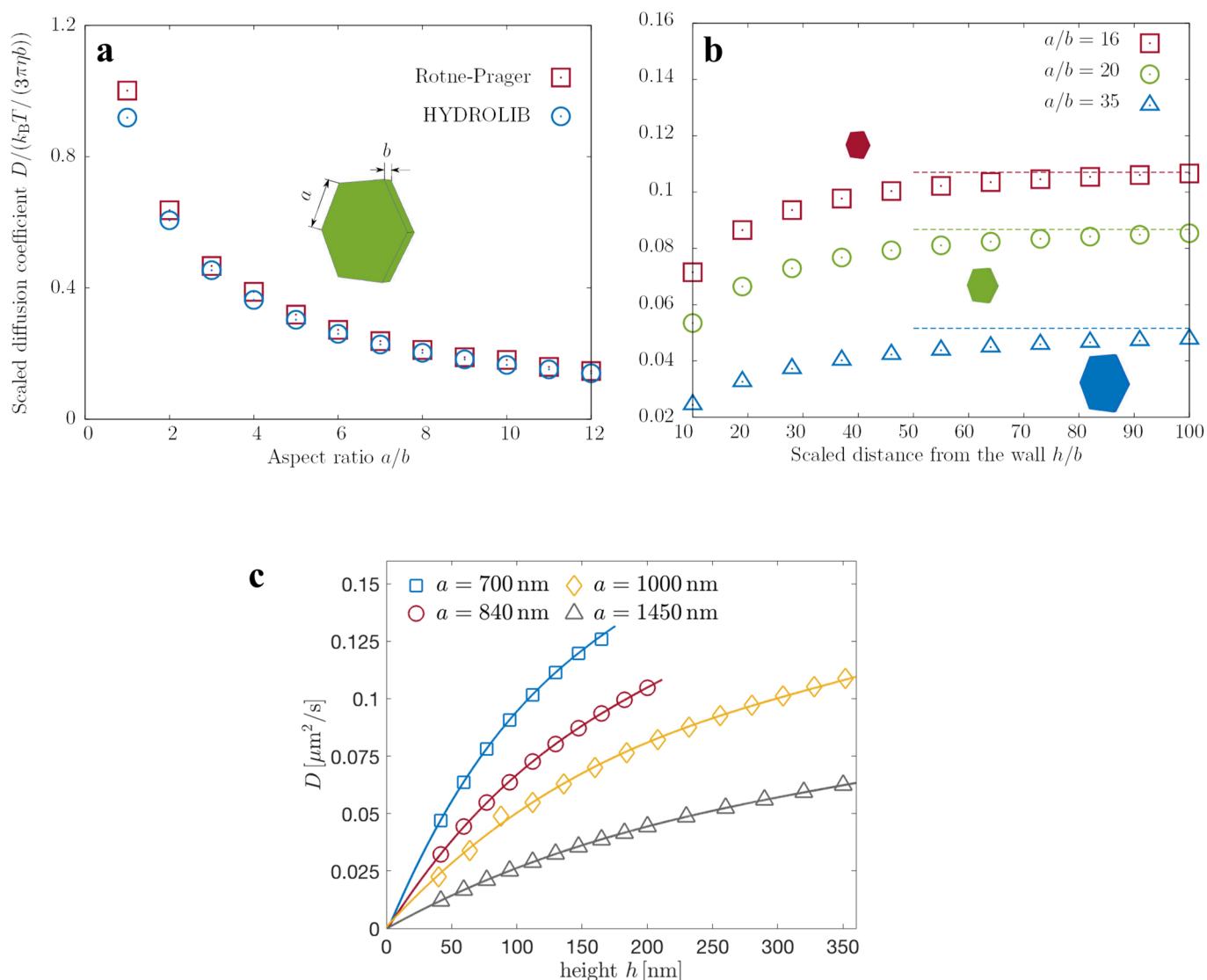
Extended Data Fig. 10 | Scaled diffusion coefficient for edgewise translational motion of a flake composed of a conglomerate of spheres arranged on a regularly shaped hexagon in an unbounded (bulk) fluid or close to a planar hard wall. a, Comparison between the Rotne–Prager approximation employed in the present work (red squares) and the bulk diffusion coefficients obtained using the open-source software HYDROLIB (blue circles). **b**, The predictions for the scaled diffusion coefficient are obtained by using the Rotne–Prager approximation combined with the Blake solution for hydrodynamic interactions between the spheres near a hard wall. Three flake sizes of aspect ratio 16, 20, and 35 are considered, which correspond to total numbers of spheres of 817, 1261, and 3781, respectively. Horizontal dashed lines correspond to the scaled diffusion coefficient in an unbounded fluid medium, that is, in the absence of the confining wall given by the substrate. **c**, Hydrodynamic simulations of a regular hexagon with various particle sizes: simulated diffusion constant D for hexagonal particles with side length $a = 700, 840, 1000, 1450$ nm depending on their distance to the surface h. Solid lines represent the fitting of the simulation data. See Supplementary Information Section IV for additional details.